DOI: 10.2478/fas-2023-0005
FATIGUE OF AIRCRAFT STRUCTURES
Volume 2023: Issue 15, pp. 58–89

X-RAY DIFFRACTION MEASUREMENTS FOR INCONEL 718 ALLOY ELEMENTS CREATED BY INCREMENTAL METHODS

Elżbieta Gadalińska[1], Paweł Żuk[2], Michał Bujak[2*]
[1] Łukasiewicz Research Network – Institute of Aviation,
Al. Krakowska 110/114, 02-256 Warsaw, Poland.
[2] GE Aerospace Poland, Al. Krakowska 110/114, 02-256 Warsaw, Poland.

michal.bujak@ge.com

Abstract

The work presented is the result of the implementation of diffraction measurements: phase composition and stresses resulting from additive manufacturing process of nickel superalloy Inconel 718 components print. With the help of diffraction methodologies, the key parameters from the point of view of the quality of prints and their strength were determined. The existence of individual phases in the material after printing was demonstrated, and the surface variation of the stress values was presented, showing its dependence on the geometry of the printed part – measurements were made at various points on the surface of samples with different geometries. In addition, the variation of the stress level was shown depending on the distance of the measurement point from the build platform on which the additive manufacturing process was carried out. Components were printed on the surface of a single build plate in order to study the effect of printing differently oriented samples with respect to the platform geometry, as well as the mutual effect of the temperature of samples printed first on the stress state of elements printed in subsequent steps of the procedure, and the effect of the temperature of elements printed later on the rate of temperature decrease, and consequently on the stress state, of elements printed first.

Keywords: diffraction, stress, additive manufacturing, DMLM, Inconel 718.
Article category: research article, experimental.

1. INTRODUCTION

In recent years, numerous interdisciplinary research groups have focused their efforts on the rapidly developing field of additive manufacturing (AM) (Pinkerton & Li, 2004; Wang et al., 2017), due to AM's capability to fabricate parts with complex geometries that cannot be obtained by regular manufacturing methods. Unlike traditional subtractive manufacturing processes, such as machining, AM constructs parts directly in their intended shape by consolidating the material in the form of small volumes, layer by layer (Wang et al., 2017), following CAD models. The use of additive manufacturing expands the bounds of human creativity, enabling the design of parts that perform their intended functions to a better degree and extent than before. 3D printing methods that employ a laser energy source are finding applications in the production of relatively small parts, characterized by a high complexity of sophisticated geometry. These techniques are beginning to be implemented to produce components from materials commonly used in aerospace such as titanium alloys, aluminum or nickel superalloys (Wang et al., 2017), such as Inconel 718.

Due to the fact that additive parts may be characterized by the appearance of undesirable characteristics such as excessive surface roughness, porosity, the occurrence of thermal stresses as a result of the printing process itself (Knuth, 1991), and changes in microstructure, grain size and symmetry, as well as the distribution and size of various precipitates and phases, it is crucial to rigorously evaluate these materials and the parts, including strength and fatigue testing, before a given technology can be adopted for serial production. Residual stresses cause deformation and cracking of the part after machining and heat treatment, and the fatigue strength of the component deteriorates when the surface layer has relatively high tensile stresses (Shiomi et al., 2004). This is a particularly important in fields of industry and transportation where the fatigue strength of components is a crucial aspect for ensuring safety and safeguarding human lives – as is the case, for example, in air transportation.

From the point of view of fatigue testing, it is very important that the surface stresses on specimens dedicated to these tests need to be within the appropriate range as defined by the relevant standards before proceeding to their implementation. The study by Gadalinska et al. (2019) used diffraction methods to determine the level of surface stresses introduced in the process of turning and grinding in Inconel 718 samples to be used in fatigue tests, concluding that grinding introduces the highest absolute value of compressive stresses. Moreover, by analyzing the half-widths of the diffraction reflections, significant differences in their values were observed for the surface states after turning and after grinding, suggesting that the process of grinding may affect micro-stresses, dislocation density, and grain size in the surface layer of the investigated material. Malicki et al. (2016) also estimated the level of strengthening of the material from full width at half maximum of X-ray diffractions peaks and compared the hardness of the Inconel 718 alloy before and after heat treatment.

Ferreri et al. (2020) comparatively addressed the question of phase changes of γ, γ', γ'', δ and carbide MC phases for forged specimens and specimens produced using additive methods (Laser Powder Bed Fusion – LPBF) immediately after printing and after the Hot Isotastic Pressing (HIP) procedure for Inconel 718 alloy. Neutron

diffraction was used as the main research method, verified by scanning electron microscopy. A significantly higher volume fraction of the δ phase and a significantly lower volume fraction of the strengthening γ phase were observed in the material after printing but by using the HIP procedure, than for the parts printed after the HIP procedure and forged. Ferreri et al. conclude that the LPBF process creates microstructural conditions that promote the transformation of γ″ to δ during the heat treatment of AMS 5663. In addition, they found that the δ phase in the LPBF material is much smaller and is located both at the grain boundaries and inside the grains, in contrast to the forged material, where it is coarse-grained and intergranular. In the case of HIP-treated material, slightly smaller δ and MC particle sizes contributing to more dispersion strengthening were observed after printing. An interesting and surprising observation was that despite having lower γ″ content, the LPBF material is stronger than both LPBF-HIP and wrought materials. Such behavior was rationalized by the finer grain structure in the LPBF material.

Measurement of the stresses produced by the printing process was carried out, among other things, in the work reported in the article by Shiomi et al. (2004), using the destructive method of applying a milling machine to remove layers of material of the printed part with a thickness of 0.1–0.2 mm. The next step of this measurement strategy was to measure the strain on a macroscopic scale. The measurement procedure was carried out until the entire printed part was removed. Information about the distribution of residual stresses was obtained, with tensile stresses in the surface and subsurface layers, and this effect was independent of the scanning speed of the printing process. Thanks to the applied heat treatment, Shiomi et al. managed to reduce the residual stresses by up to about 70%, while the layer-by-layer rescanning procedure reduced them by about 55%. Another proposed way to reduce the value of surface stresses was to preheat the base plate. This action made it possible to reduce surface stresses by 40%.

A comparative stress measurement methodology was employed by Mercelis and Kruth (2006) for SS316L stainless steel parts made by SLS and SLM methods. Two methods were used: the crack compliance method and the method using the X-ray diffraction phenomenon. The experimental methods verified model calculations. The experimental results in the paper confirm previous reports of tensile stresses just below the top surface, followed by a significant zone of compressive stresses. The authors report that the factors determining the magnitude of the stresses are the height of the element and the height and stiffness of the base plate. The strategy of the printing process will also be a factor affecting the stress values: the stresses will be higher for the direction perpendicular to the scanning direction, but lower for the direction in line with the scanning direction. If the island strategy is used, the value of the maximum stress will be lower while the stresses for mutually perpendicular directions will not show significant differences. Two strategies have been suggested to reduce residual stresses resulting from the printing process: heat treatment using a laser source and heating the base plate.

The microstructure and residual stresses for the Inconel 718 superalloy were also studied for the rapid laser-fed (LRFed) process by Liu et al. (2011). The microstructure of the tested printouts showed the appearance of columnar dendrites growing epitaxially

along the direction of the print. After annealing at high temperature, the geometry of the dendrites changed – equiaxed grains were formed. Stresses were measured using the Vickers microindentation method. The authors concluded that the residual thermal stresses are distributed unevenly (they are high in the overlapping areas of two adjacent transitions and low in the inner areas of a single transition), and thus play a significant effect on recrystallization during solution annealing.

A very detailed analysis of the microstructure is reported by Amato et al. (2012), where the effective phase composition and formation of precipitates were analyzed for prints produced from Inconel 718 alloy by selective melting of powder in an argon or nitrogen atmosphere from pre-melted powder. First, for printed parts (here in the form of cylinders) not subjected to any additional treatment, the occurrence of columnar grains and arrays of γ' phase (Ni_3Nb, body-centered tetragonal) with strong texture on the direction was observed. After application of the HIP process, the texture of the coagulation phase sharpened while the material partially recrystallized, adopting the FCC structure. After annealing, half recrystallization and the appearance of spheroidal γ' phase precipitates occurred. The appearance of δ phase precipitates both before and after recrystallization was also observed. The hardness measurement showed that the hardest material was the one after the HIP process, followed by the annealed one, while the as-built material had the lowest hardness.

From an economic and environmental point of view, one of the most important aspects during the manufacture of components by incremental methods is the recyclability of the powder used in such manufacturing procedures. Ardila et al. (2014) addressed this issue with regard to powder made of Inconel 718 alloy, finding that the state of the powder does not undergo significant changes during reuse for the manufacture of components by incremental methods. The authors report that most of the particles remained spherical and, moreover, there was no significant increase in the defective morphology of the powders. In addition, the particle size distribution remained constant even after several manufacturing processes, except for a small number of particles aggregated to sizes of 50 to 100 microns. One very interesting observation was that although the prints were made in a chamber where oxygen (2000 ppm) was present, the composition of the powder did not change. As a result, even after 14 production iterations, the samples obtained from the printing process did not differ from each other in either the metallurgical or the mechanical context.

Researchers involved in the development of printing procedures are aware of the affinity of modern 3D manufacturing methods with welding processes, since both methods use an increase in process temperature to achieve the desired result, i.e., the formation of a weld/join between two parts or the formation of a part with any level of shape complexity. Significant temperature gradients cause significant changes in microstructure properties. As early as 1996, Huang et al. (1996) addressed the effect of homogenization temperature on microcracks in heat-affected zones (HAZ) for Inconel 718 superalloy after electron beam welding. It was observed that the tendency of microcracks in the heat-affected zone of the electron-beam-welded Inconel 718 casting (determined by total crack length – TCL measurements) first increases and then decreases as the homogenization temperature increases from 1037°C to 1163°C. The minimum TCL value was observed in the sample homogenized at 1066°C. Moreover,

it was observed that the volume fraction of the δ-Ni_3Nb and Laves phase decreases with increasing homogenization temperature, but the volume fraction of MC carbide remains constant over the entire homogenization temperature range.

Radhakrishna and Prasad Rao (1997) sought to identify the morphology and composition of the Laves phase in areas near welds in Inconel 718 alloy. They found that the deleterious Laves phase tended to appear in interdendritic areas after the weld was made. This occurs as a result of microsegregation of alloying elements during weld solidification. The factor with the most significant effect on the morphology and composition of this phase was the cooling rate of the weld. High cooling rates proved to be much more favorable than low rates.

Blackwell (2005) compared microstructural and mechanical properties for Inconel 718 alloy prints manufactured by the LENS method in the as-built condition and after HIP treatment. The main objective of this study was to examine the effect of the HIP process on the properties of printed parts. The process was found to lead to a decrease in anisotropy in the printed element, but generated a significant increase in grains in the substrate.

Ghorbanpour et al. (2022) addressed the effects of printing parameters and heat treatment for functionally graded additionally manufactured elements obtained from the nickel superalloy under discussion by laser powder sintering on the microstructure and indirectly on fatigue crack growth. Laser power, scanning speed, unit layer thickness, laser inter-path distance, and beam distribution function were changed during the printing of the test specimens. In addition, the prints were carried out using different orientations of the print direction with respect to the geometry of the samples. After printing, the samples were subjected to various post-process thermal and thermal treatments associated with the HIP procedure. The properties of the samples were compared with analogous forged and printed parts, but for which no heat treatment was performed. It was observed that the tested samples differed significantly in terms of porosity, grain size, grain shape, content of strengthening and deleterious phases. To study the fatigue properties, the samples were subjected to three-point bending tests. The experiments showed that heat treatment could increase the damage tolerance of L-PBF Inconel 718 parts to the level of forged material. Interestingly, the effect of crack closure-induced roughness was found to be a function of the orientation of the structure, especially in the low stress-ratio regime. The study found that by using an appropriate post-treatment procedure, fatigue behavior can be improved to a level even higher than that of forged material. The results of the current study can be used as a benchmark for determining the most effective heat treatment, given the applications of functionally graded materials. In addition, Ghorbanpour et al. stated that although the results of their study are comprehensive with regard to fatigue crack growth at room temperature, further research is needed at higher temperatures.

Hönnige et al. (2021) studied the influence of printing parameters in the L-PBF process, such as temperature cycling, thickness of the layer applied at one time and post-process heat treatment. The main focus of this work was to study the effect of the choice of printing parameters on microstructure and residual stresses. As in many similar studies, the formation of dendritic grains in the microstructure of prints and the existence of Laves phases in interdendritic areas were observed. The neutralization

of microstructural anisotropy was achieved by applying annealing thermal treatment while the Laves phase was thus partially dissolved in the basic γ-matrix. A change in morphology from coarse-grained to discrete particles was achieved by thermal annealing processes. After the annealing thermal treatment, the samples had lower compressive residual stresses in the mean and maximum values, which should be related to the evolution of the microstructure during the annealing thermal treatment. The microhardness values of L-PBF Inconel 718 parts are comparable with literature data.

Previous works has also investigated changes in microstructural features, phase formation and three-dimensional variation of the state of stress resulting as an effect of the implementation of printing with the use of the WAAM method, which allows the manufacture of parts of larger sizes, but characterized by a lower complexity of geometry than in the case of laser methods. One such work, describing in great detail the changes in microstructure and mechanical properties, is Hönnige et al. (2021). Diffraction measurements were used to determine the three-dimensional stress state under different manufacturing conditions. Inter-pass rolling was found to have a significant effect on reducing the values of deformation of the resulting part. It was shown that near the printing platform the values of stresses had a tensile character, while on the surface of the printed part the stresses assumed a compressive character. Another positive effect of using the inter-pass rolling procedure during printing was the alleviation of the disordered Laves phase, whose high concentration of niobium usually prevents it from being re-solved, and a reduction in grain size and crystallographic texture. Another advantage of inter-wall rolling, Hönnige et al. report, lies in the method's potential to reduce the porosity of post-printed parts.

For many years, researchers have struggled with the problem of reliably measuring the absolute values of residual stresses of components with complex shapes. Unfortunately, this is often a methodological problem, and in the case of printing, the surface roughness also has a significant impact on the results of measurements by diffraction methods. Since diffraction methods are the only non-destructive methods that make it possible to obtain information about the absolute value of stresses, the present study strives to identify their values on samples produced in DMLM technology.

2. MOTIVATION

The main motivation behind the diffraction experiments we carried out on components made from Inconel 718 alloy using incremental technologies was to identify the level of stress occurring in the samples as a result of the additive manufacturing process.

In general, components produced using additive methods are characterized by surface tensile stresses, high porosity and significant roughness of the final component. All these features are undesirable phenomena and therefore require control and levelling. Diffraction methods are an excellent tool for obtaining information on the absolute values of residual stresses on the surface of final printed parts using the classic, standardized $\sin^2\psi$ method. Research potential can also be seen in the application of methods such as the small angle X-ray scattering (SAXS) method for determining

the porosity of printed parts and the reflectometry method, which in turn makes it possible to define the level of roughness.

This paper presents the results of diffraction measurements of the phase composition using the Rietveld methodology and the results of stress measurements using $\sin^2\psi$.

3. MATERIAL AND SPECIMENS

3.1. Material

Nickel superalloys, such as the Inconel 718 alloy studied herein, have unique properties such as excellent refractory and high corrosion resistance in various, even extreme temperature ranges Gadalińska et al. (2019). These alloys are also characterized by high wear resistance, special magnetic properties and significant electrical resistance. They also have an almost zero coefficient of temperature expansion in the range from 0°C to 100°C (Gadalińska et al., 2019). As such, they also have excellent creep properties (Wang et al., 2017). From the chemical point of view, it is noteworthy that the Inconel alloys are resistant to chlorine and fluorine, exhibit oxidation resistance up to 1100°C and in oxidation-sulfur atmosphere up to 850°C (Wang et al., 2017; Gadalińska et al., 2019). Thanks to these unique properties, Inconel alloys are used in the manufacture of steam and gas turbines, as well as parts for the aerospace and nuclear industries, as the extreme conditions encountered there do not affect the properties of alloys of this type.

The chemical composition of Inconel 718 alloy includes elements such as chromium, iron, molybdenum, tungsten and tantalum, thanks to which the alloy is characterized by exceptional strength. The addition of aluminum and titanium ensures high strength of this alloy in high-temperature conditions. In addition, aluminum has a preventive effect under corrosive and oxidizing conditions. A similar effect is achieved with the addition of chromium and tantalum. Excellent creep properties are achieved by additives such as boron, carbon and zirconium (Gadalińska et al., 2019; Ezugwu, 2004). The chemical composition of this particular alloy (Inconel 718) w% is 0.040 C, 0.006 P, 0.002 S, 0.15 Si, 0.05, Mn, 19.15 Cr, 52.46 Ni, 3.04 Mo, l0.40 A, 1.08 Ti, 0.002 B, 4.94 Nb, 0.002 Mg (Yao et al, 2013). Heat treatment applied to Inconel 718 results in the formation of precipitations and provides a high concentration of carbides at grain boundaries. Thus, the movement of dislocations is hindered as the value of tensile strength and yield strength is increased. The tensile strength of this material is 1489 MPa, yield strength is 1319 MPa, elongation is 20%, shrinkage is 46%, and the hardness of the material is 468 HV (Yao et al, 2013; Sharman et al., 2006). The main crystalline phase of this alloy is a solid solution phase of Fe, Cr and Mo in nickel crystallizing in an austenitic FCC matrix phase (Gribbin et al., 2019). There are also secondary phases in the alloy that also have a significant impact on mechanical properties (Sharman et al., 2006). These are the γ' (coherent spherical Ni_3Al particles 10 to 40 nm in diameter) and γ'' (homogeneously distributed disc-shaped Ni_3Nb particles with a tetragonal crystallographic structure) strengthening phases (Ghorbanpour et al., 2022; Hosseini & Popovich, 2019). Unfortunately, Inconel 718 alloy also contains phases with disorderly effects from the point of view of strength and fatigue properties (Suui et al., 2017), such as hexagonal Laves phase $(Ni,Fe,Cr)_2(Nb,Mo,Ti)$, orthorhombic δ (Ni_3Nb) and MC

carbides (Ghorbanpour et al., 2022; Hosseini & Popovich, 2019). A brittle Laves phase of irregular shape and micron size is formed at the end of the solidification process due to microsegregation of alloying elements (Ghorbanpour et al., 2022; Popovich et al, 2017). Due to the low rate of Nb diffusion in the γ matrix, Laves phases tend to form at grain boundaries and in interdendritic areas (Nezhadfar et al, 2020; Ghorbanpour et al., 2022). The δ phase forms needle-shaped precipitations ranging in size from 1 to 8 μm (Burke & Miller 1991). The presence of this phase causes a decrease in strength properties, albeit without contributing to a deterioration in creep strength (Sanchez et al, 2021). The properties of Inconel 718 alloy are similarly affected by rough, brittle carbides (Ghorbanpour, 2022; Mostafa, 2017). The main disadvantage of Inconel 718 alloy is its low machinability, which is mainly due to the low thermal conductivity of this material (11.4 W/m/K) (Gadalińska et al., 2019; Sharman et al., 2006).

3.2. Specimens

To determine the properties of Inconel 718 prints by means of diffraction methods, two sets of samples were prepared. The experiments that yielded data on the phase composition of the samples were carried out with the cubic and cylindrical samples presented in Figure 1.

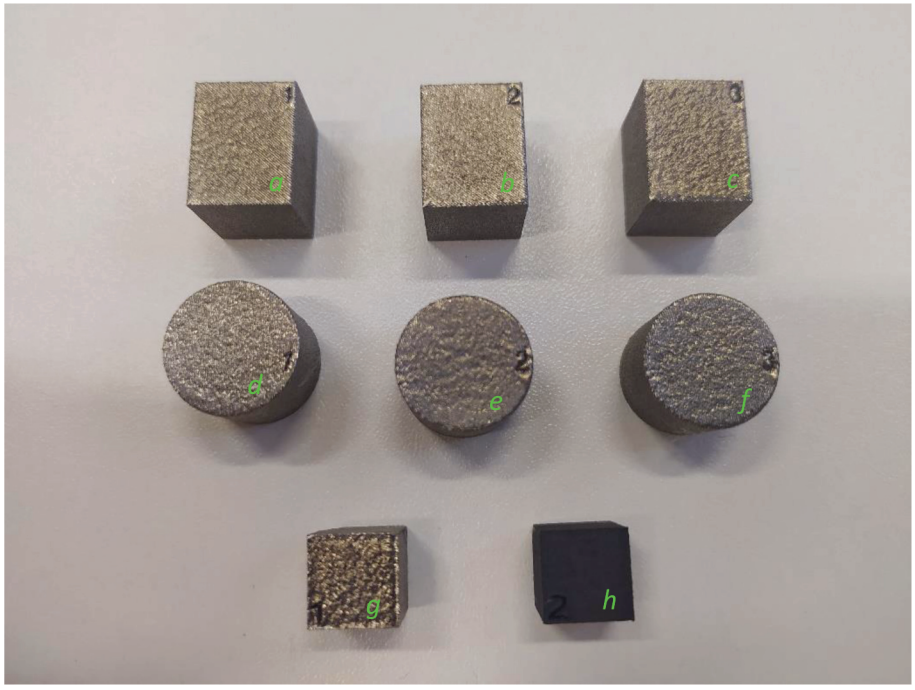

Figure 1. Specimens used in the X-ray diffraction phase analyses.

The intention of the stress diffraction measurement was to obtain information about the distribution of stresses on the surface of samples of various shapes, ranging from cuboidal to those that mimicked the shape jet engine components. In addition, the purpose of the series of experiments was to determine the effect of printing direction on microstructural and mechanical properties, as well as the effect of heat from individual samples printed on one platform on neighboring components that were

chronologically printed further down the line. Samples for which stress measurements were realized are shown in Figure 2. To perform diffraction measurements of the stresses and minimize the effect of cutting off the elements from the platform on the potentially possible relaxation of residual stresses, which are a remnant of the printing process, it was decided to cut the platform itself, without severing the printed samples from the build plate (see Figure 2).

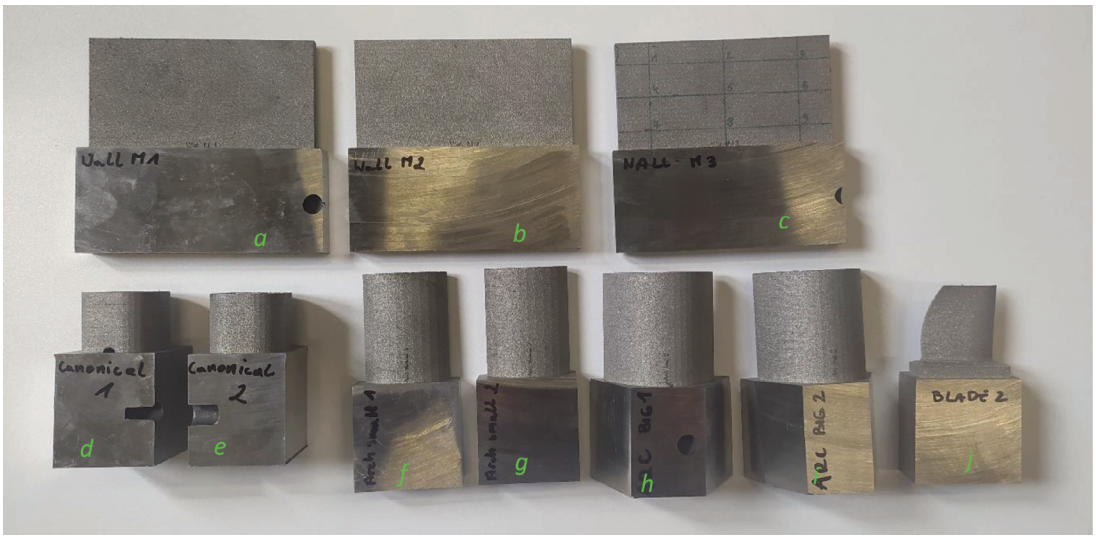

Figure 2. Specimens used in the X-ray stress measurements.

4. X-RAY DIFFRACTION EXPERIMENTS

4.1. Phase composition

Phase composition measurements were carried out for two specimens of two types with different geometries: cubic specimen (labelled g, Figure 1) and wall specimens (labelled a–c, Figure 2) after being cut off from the platform. The measurement was repeated for a sample of larger size (wall shaped), to allow the appropriate slits to be used to form a beam of larger dimensions and thus make the measurement more accurate. In addition, the measurement range of 2θ degrees for the wall-type specimens (a–c in Figure 2) was extended to about 154 degrees in order to capture and index diffraction reflections, which will be suitable for stress measurements on components in the next steps. Such a procedure also made it possible to optimize the measurement parameters for stress measurements. The experiments were performed in classical Bragg-Brentano diffraction geometry using a proportional detector. The use of the proportional detector was intended to try to capture diffraction reflections becoming from described in the literature and the expected precipitations. The full diffractogram was acquired using a copper anode X-ray tube generating radiation with a characteristic radiation wavelength $K_{\alpha 1}$ of $\lambda = 1.540598$ Å. In the path of the incident beam the lenses focusing and generating a quasi-parallel beam in both planes were applied to avoid problems generated by the roughness of the printouts. The K_{β} component of the copper tube radiation was removed by using a nickel filter. The result of the Rietveld phase analysis is presented below in Table 1.

Table 1. Rietveld phase analysis results.

phase **percentage [%]**	**ICDD card number**	**crystallographic structure**	**lattice parameter [Å]**
$Fe_{0.5}Ni_{0.5}$ 89.1%	04-021-6318	cubic, Fm-3m, 225	$a_0 = 3.59458$
$Nb_{0.1}Ni_{0.9}$ 3.5%	04-004-4494	cubic, Fm-3m, 225	$a_0 = 3.803844$
$NbNi_3$ 3.3%	04-012-8012	tetragonal, I4/mmm, 139	$a_0 = 3.566829$, $c_0 = 7.39813$
$NbNi_3$ 2.6%	03-065-2589	orthorhombic, Pmmn, 59	$a_0 = 4.308615$, $b_0 = 5.165817$, $c_0 = 4.573394$
Ni_3Ti 0.6%	01-075-0878	hexagonal, P63/mmc, 194	$a_0 = 5.1114773$, $c_0 = 8.313766$
$Ti_{0.33}Ni_{0.67}$ 0.4%	04-007-1996	rombohedral, R-3m, 166	$a_0 = 2.550052$, $c_0 = 43.62515$
Cr_2Nb 0.5%	04-004-6470	cubic, Fd-3m, 227	$a_0 = 6.989395$

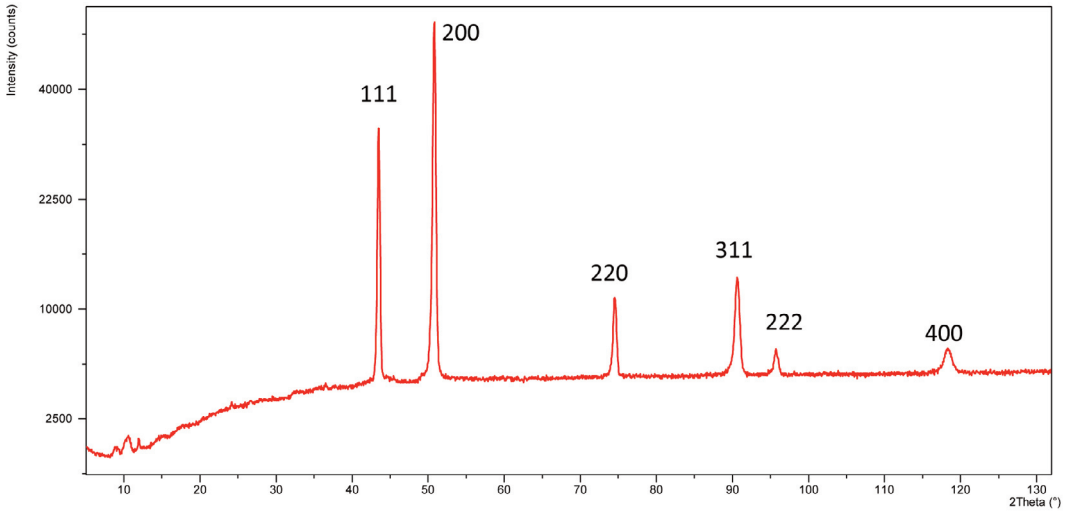

Figure 3. Diffractogram obtained for the cubic specimen (g in the Figure 1). The individual reflections of the dominant phase were described by the Miller coefficients hkl.

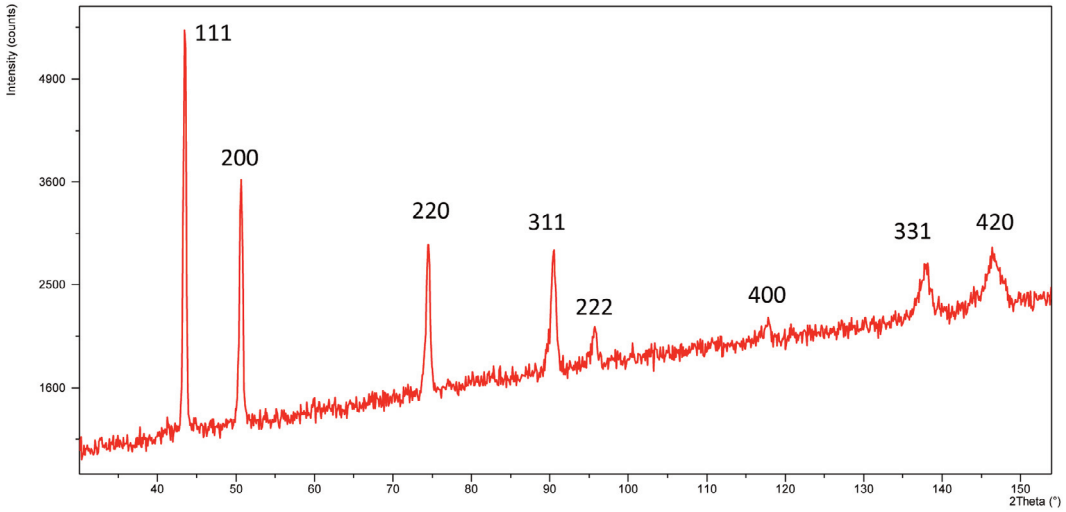

Figure 4. Diffractogram obtained for wall type specimen (geometry like a–c in Figure 2) cut off from the platform. The individual reflections of the dominant phase were described by the Miller coefficients hkl.

The analysis shows the existence of a dominant phase with a face centered cubic FCC structure: $Fe_{0.5}Ni_{0.5}$. A component of phases built up by nickel and niobium compounds with different crystallographic structures (totaling about 9.4%) was also observed: cubic, tetragonal, orthorhombic structure. In addition, small amounts of phases that are compounds of nickel with titanium and niobium with chromium were found to be present.

4.2. Stress measurements

Stress measurements were carried out using the standard $\sin^2\psi$ method (Standard EN 15305:2008; Hilley, 1971) with a MALVERN PANalytical Empyrean X-ray diffractometer. In the measurement, the same assemblies (X-ray tube, polycapillary lens and filter) were used in the incident beam path as in the phase composition measurement. Radiation detection was performed using a PIXcel1D semiconductor detector.

The stress measurements parameters were first optimized for a wall-shaped specimen used at first for phase composition measurements. The second aim of the first set of measurements was to estimate the influence on the stress state made by cutting the print off the platform. The measurements were programmed to produce two diffraction reflections, with Miller coefficients of {331} and {420}. This allowed the target set of measurement parameters to be based on only one, more optimal solution. The measurement parameters needed to be optimized in terms of the specimen's geometry; moreover, the specimens designated by letters d–j in Figure 2 possessed curvature with the potential to complicate the measurements. All stress measurements were carried out for two mutually perpendicular directions in relation to the geometry of the specimens. For the wall-shaped specimens these were the 'longitudinal' and 'transverse' directions (see Figure 5) while for the specimens of curved geometry, like for specimens showed in Figure 2 d–j, the directions of measured stresses were defined by the words 'axial' and 'circumferential'.

The procedure for converting crystal lattice strain values into stresses was the same for all samples. The linear nature of the background accompanying the diffraction reflections was assumed and the Lorentz-Polarisation correction procedure was applied, assuming neglected crystallographic texture and a significant broadening of the reflections resulting mainly from the notable refinement of the coherently scattering domains. The procedure for subtracting the $K_{\alpha 2}$ component of the characteristic radiation was realized using the Rachinger method. The relative position of the diffraction reflections was determined using a modified Lorentzian function. During the analysis, the following values of the components of the stiffness tensor were assumed: $s_1 = -1.62 \;\; 1/TPa$ and $\frac{1}{2}\, s_2 = 7.14 \;\; 1/TPa$ (Prevey, 1986).

Preliminary measurements before and after being cut off the platform

Preliminary stress measurements were taken for the wall-shaped specimen for 9 points defined in Figure 5. The measurements were carried out for two directions along the long side of the specimen ('longitudinal') and the short side of the specimen ('transverse'). For some points, measurements were not performed for all directions (the measurements 'transverse' direction was omitted for points 1, 4, 5, 7 before cutting off the specimen from the platform) due to geometrical limitations of being able to place the sample in the axis of the goniometer for these points and for this measurement direction. Nevertheless, the range of measurements carried out does allow meaningful conclusions to be drawn from the measurements before and after the sample was cut off from the platform.

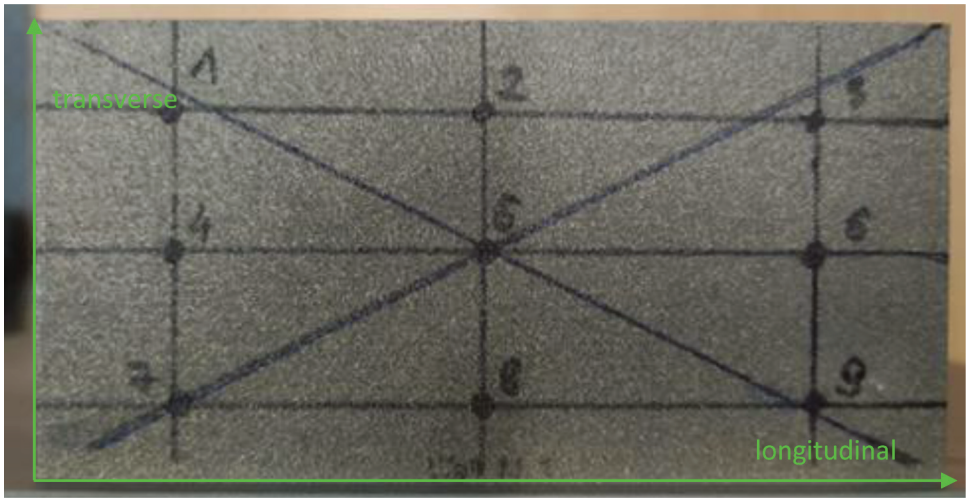

Figure 5. Wall-shaped specimen with location of measuring points for preliminary measurements before and after being cut off from the printing platform.

The results of the measurements before and after cutting from the platform for wall-shaped specimen are shown in Table 2 and in Figure 6, Figure 9.

Table 2. Results of X-ray diffraction stress measurements for the wall-shaped specimen.

before cut					**after cut**			
point no. ↓	longitudinal		transverse		longitudinal		transverse	
	σ [MPa]	Δσ [MPa]	σ [MPa]	Δσ [MPa]	σ [MPa]	Δσ [MPa]	σ [MPa]	Δσ [MPa]
1	7.1	25.1	-	-	-13.6	90.4	-332.7	48.7
2	-6.3	16	100.5	31.4	187.9	23.3	46.5	30.2
3	-55.6	27.5	132.6	16.3	136.1	21.2	-22.1	42.7
4	1.9	22.5	-	-	96.5	19	-16.9	36.6
5	-53.1	14.9	-	-	110.3	35	-4.2	29.7
6	-34.6	14.2	95.1	29.8	110.8	23.5	-29.2	24.4
7	13.6	15.5	-	-	184.5	112.2	298.1	115.6
8	-55	20.1	107.4	79.5	139.4	29.6	49.7	33.6
9	-11.1	26.7	160.8	58.6	168.1	154.5	102.6	21.5

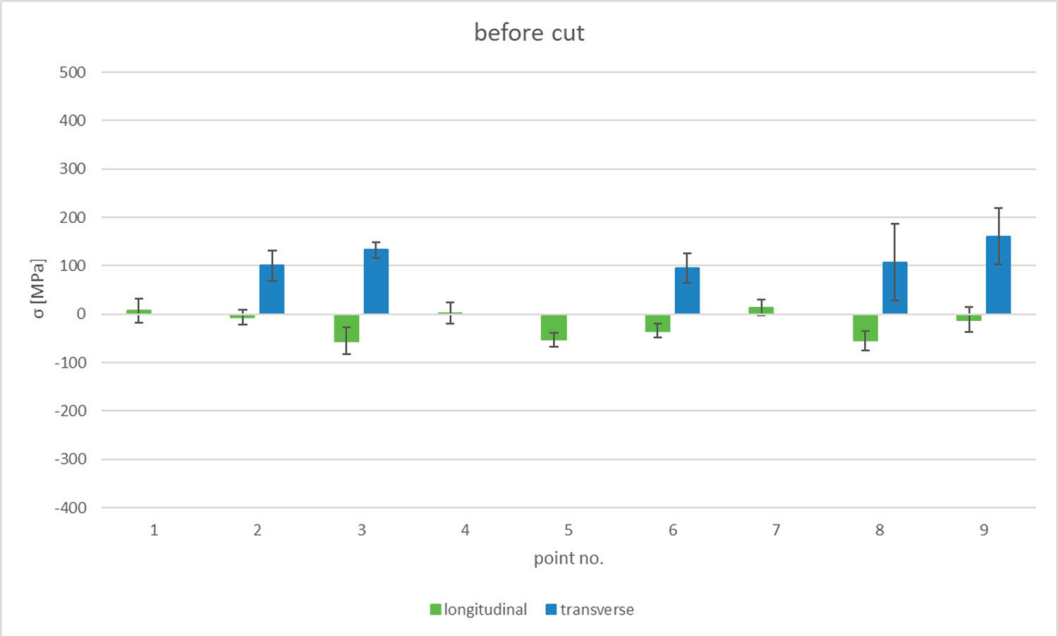

Figure 6. Results of X-ray diffraction stress measurements for wall-shaped specimen before being cut off the built platform.

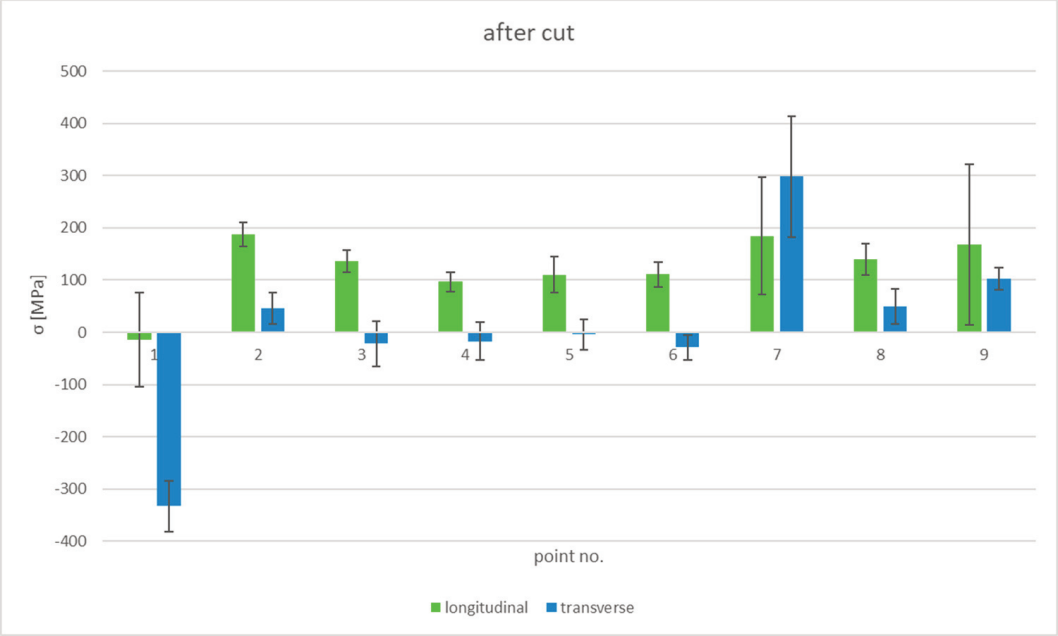

Figure 7. Results of X-ray diffraction stress measurements for wall-shaped specimen after being cut off the built platform.

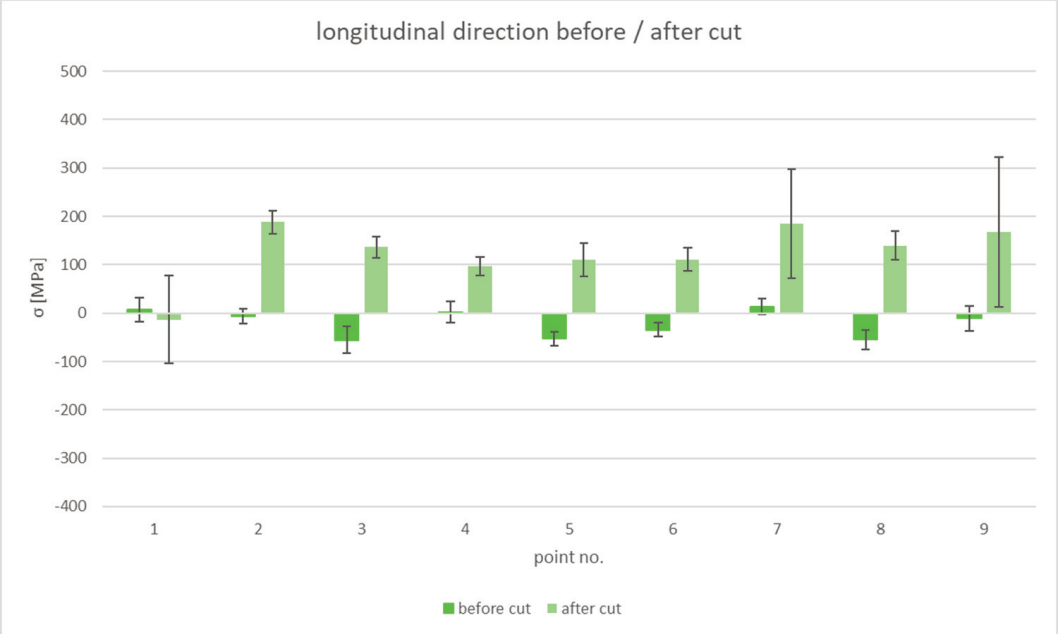

Figure 8. Comparison of results before and after being cut off from the platform – measurements performed in longitudinal direction.

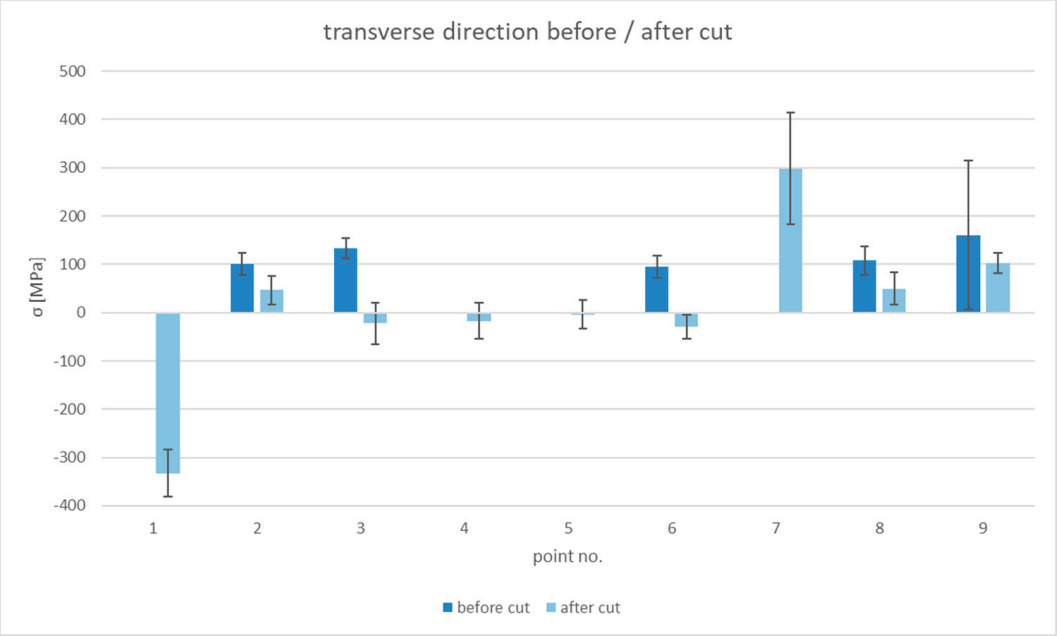

Figure 9. Comparison of results before and after being cut off from the platform – measurements performed in transverse direction.

Before the specimen was cut off from the print platform, almost zero negligible stress values were observed for the 'longitudinal' direction while tensile stresses with values in the range of 100–200 MPa were seen for the 'transverse' direction. After the specimen was cut off from the print platform, the stresses for the 'longitudinal' direction changed: they took on the character of tensile stresses with values of approximately 100–200 MPa. In the case of stresses in the 'transverse' direction, a levelling off of tensile stress values was observed for points 2 and 3 and in the central part of the specimen: points 4, 5 and 6. A change in stress values was also observed for points close to the platform. For the point extreme to the platform (point 1), compressive stresses of approximately –350 MPa were measured after the specimen was cut off. Unfortunately, the lack of a measurement result for this point before the specimen was cut off from the platform does not allow conclusions to be drawn in this case.

Measurements carried out before and after the cut-off from the print platform led to the conclusion that the cut-off results in a significant change in the stress distribution and cannot be applied when trying to carry out stress measurements using diffraction methods. The above measurement cycle allowed for the optimization of measurement parameters and a fivefold reduction in measurement time for one point and one measurement direction.

Measurements were carried out for 10 specimens presented in Figure 2 and a total of 92 measurement points were measured, with measurements for the majority of them being carried out for two mutually perpendicular measurement directions. As a result, 178 measurements were carried out.

Stress measurements for the wall-shaped specimens

For the three wall-shaped specimens, labeled WALL M1, WALL M2 and WALL M3 (a–c in Figure 2), measurements were carried out on 12 points, as illustrated in Figure 10 for specimen WALL M1.

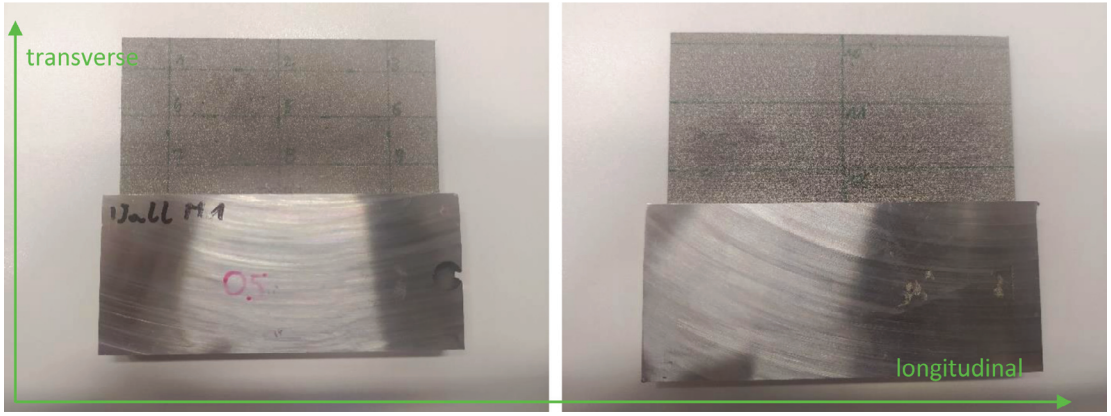

Figure 10. Specimen WALL M1, showing the location of measuring points on both sides.

The results obtained for the wall-shaped specimens are presented in Table 3 and in Figures 11–13.

Table 3. Results of X-ray diffraction stress measurements for wall-shaped specimens.

	WALL M1				WALL M2				WALL M3			
point no. ↓	longitudinal		transverse		longitudinal		transverse		longitudinal		transverse	
	σ [MPa]	Δσ [MPa]	σ [MPa]	Δσ [MPa]	σ [MPa]	Δσ [MPa]	σ [MPa]	Δσ [MPa]	σ [MPa]	Δσ [MPa]	σ [MPa]	Δσ [MPa]
1	277.2	170.3	275.2	97.9	267.7	166.4	399.9	110.8	194.2	171.1	325.3	158.6
2	289.4	153.2	253.1	104.8	440.9	180.3	304.3	94.9	285	198	333.7	173.7
3	271.6	172	259.4	90.6	461.4	200.7	320.7	123.5	247.6	180.8	293.1	189
4	231.7	296.5	345.5	163.1	249	196.9	387.8	166.3	229.2	165.3	346.6	172.9
5	252.5	303.3	579	190	451.1	165.2	432.9	152.6	-42.7	28.8	319	186.9
6	235.4	174.6	314.6	168.3	254.4	205.4	347.4	166.6	-45.4	12.8	385.7	129.7
7	213.8	288	318.6	198.4	493.5	198.8	532.3	157	210.9	161.9	309.4	114.8
8	295.6	290.8	364.5	180.3	246.4	186	415.2	167.5	-6.8	32.1	232.6	84.7
9	221.9	116.8	337	201.7	479.2	180	403.5	159.7	-56.8	18.4	276.8	127
10	279.9	173.9	358.4	172.2	277.8	204.6	367.7	190	99.6	40.9	381.1	177.6
11	230.3	130.3	406.6	192	206	177.1	367.3	198.9	22.6	34.6	403.2	161
12	221.9	199.3	420.7	89.2	284.4	174.4	306.3	172.7	190.7	81.1	371.9	62

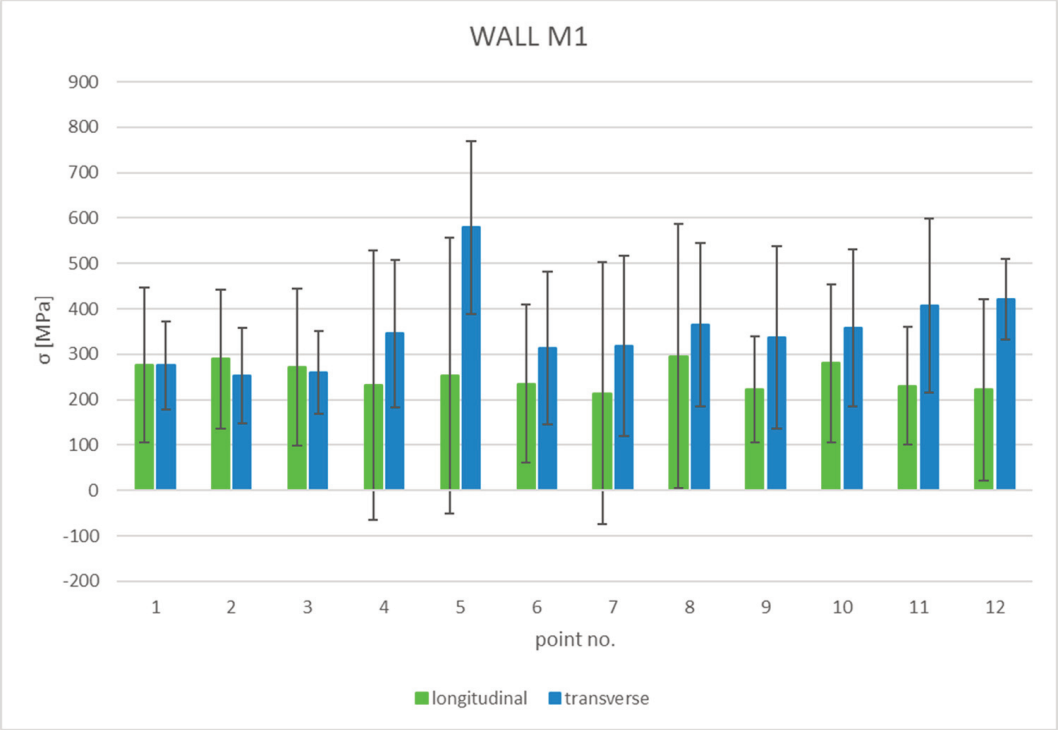

Figure 11. Results of X-ray diffraction stress measurements for specimen WALL M1.

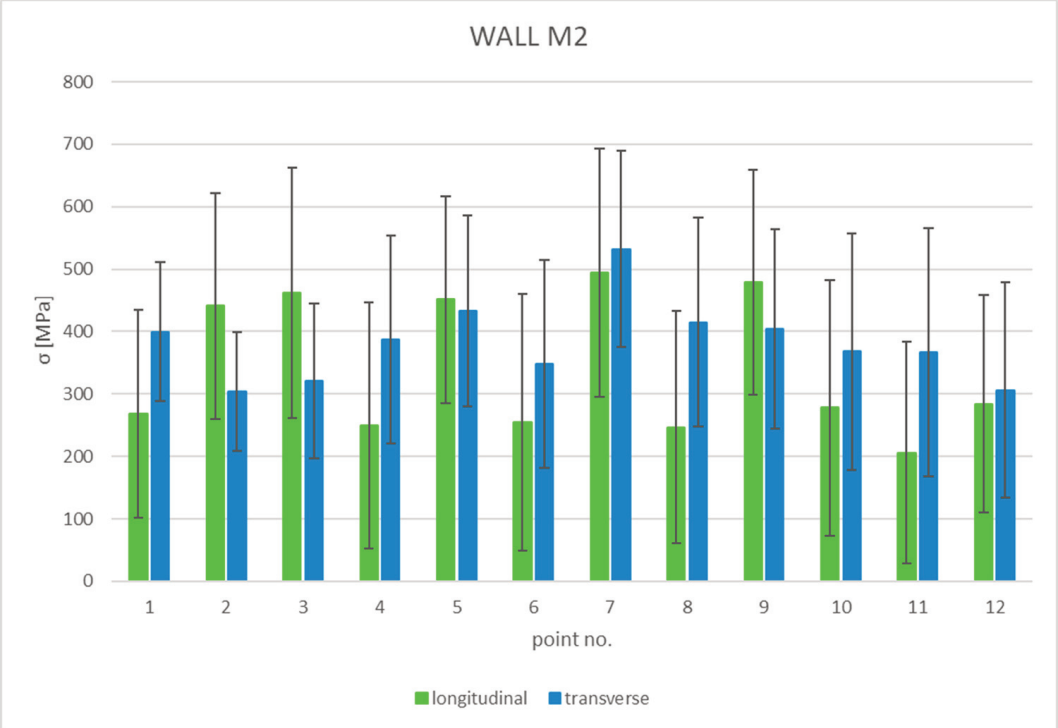

Figure 12. Results of X-ray diffraction stress measurements for specimen WALL M2.

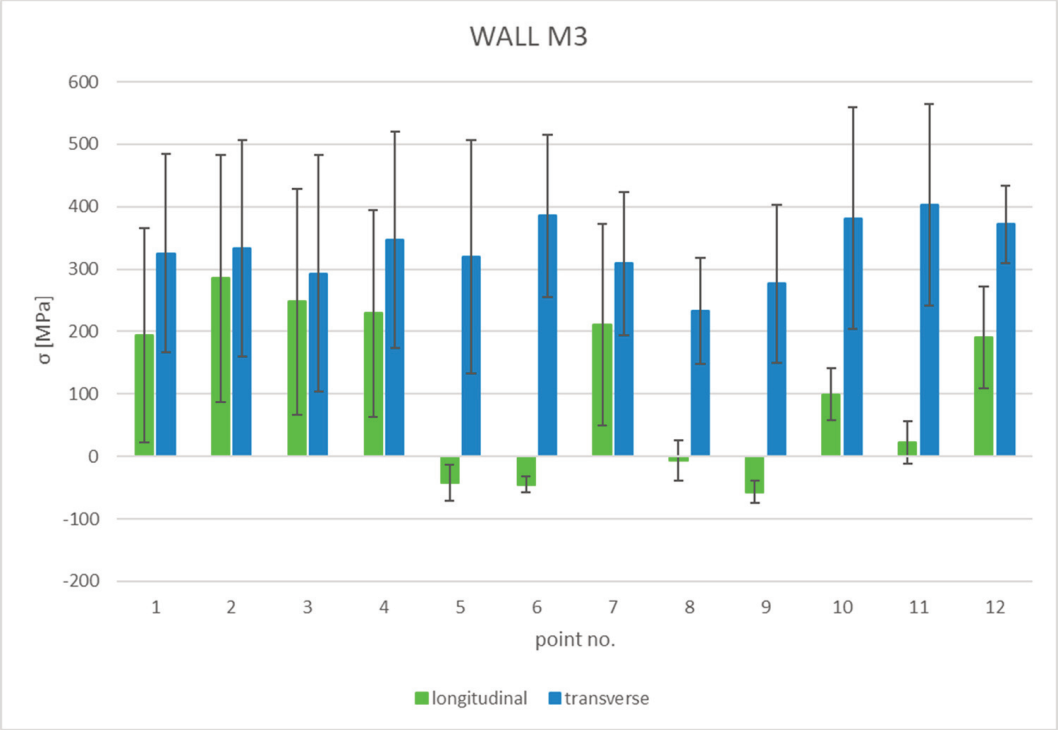

Figure 13. Results of X-ray diffraction stress measurements for specimen WALL M3.

Stress diffraction measurements for specimen WALL M1 indicate the occurrence of tensile stresses for both directions measured, with higher values for the 'transverse' direction. For the 'longitudinal' direction, values in the range of approx. 200 MPa to 300 MPa were obtained, while for the 'transverse' direction the values ranged from approx. 250 MPa to 600 MPa. The highest value was obtained for the center point of the specimen (no. 5).

Specimen WALL M2 also showed tensile stresses of a comparable range to that of WALL M1. There was no trend of higher values for either direction. In general, the values varied from approx. 200 MPa to approx. 500 MPa.

Stress diffraction measurements for specimen WALL M3 showed the existence of stresses of a tensile nature for the 'transverse' direction for all points. These values ranged from about 200 MPa to 400 MPa, a slightly narrower range than for WALL M1 and WALL M2. In the case of this specimen, there was a change in the stress values for the 'longitudinal' direction: for most of the points, the stress values took on values ranging from about 100 MPa to 300 MPa while for points in one particular area, including points 5, 6, 8, 9, 11, the values were close to zero or took on small values of a compressive nature.

Stress measurements for the canonical specimens

For the two CANONICAL type specimens, 11 measurement points and 2 perpendicular measurement directions ('axial' and 'circumferential') were defined. The location of points is presented in Figure 14.

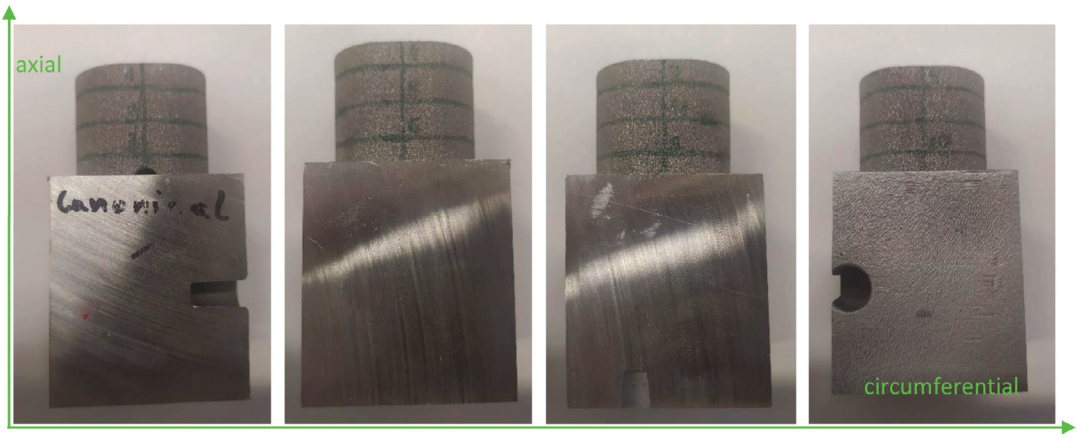

Figure 14. Specimen CANONICAL 1, showing the location of measuring points on all sides.

The results obtained for the two canonical-type specimens are presented in Table 4 and in Figures 15–16.

Table 4. Results of X-ray diffraction stress measurements for canonical shaped specimens.

point no. ↓	CANONICAL 1				CANONICAL 2			
	axial		circumferential		Axial		circumferential	
	σ [MPa]	Δσ [MPa]	σ [MPa]	Δσ [MPa]	σ [MPa]	Δσ [MPa]	σ [MPa]	Δσ [MPa]
1	351.6	190.6	36.6	108.3	335.7	175.7	121.1	173.8
2	314.8	173.4	98.9	130.8	457.6	143.9	65.4	62.8
3	188.4	85.5	38	118.5	108.5	138.2	52.1	55.1
4	304.2	166.4	-7.7	130	513.9	171.1	51.1	72.1
5	316.1	191.4	115.9	145.8	306.5	182.6	113.2	144.2
6	-70.2	97.6	21.2	66.7	199.7	61.3	62.6	105.5
7	373.8	166.2	61.7	76.2	372.9	174.1	43.8	82
8	93.6	130.4	102.1	97.3	292.1	41.2	72.2	127.8
9	347.8	182	49.3	106.8	208.5	52.5	51.7	92.6
10	-78.8	71.6	50.8	99.5	363.4	157.1	89.4	106.4
11	383.9	191.4	174.1	148.1	378.5	197.9	138.7	118.7

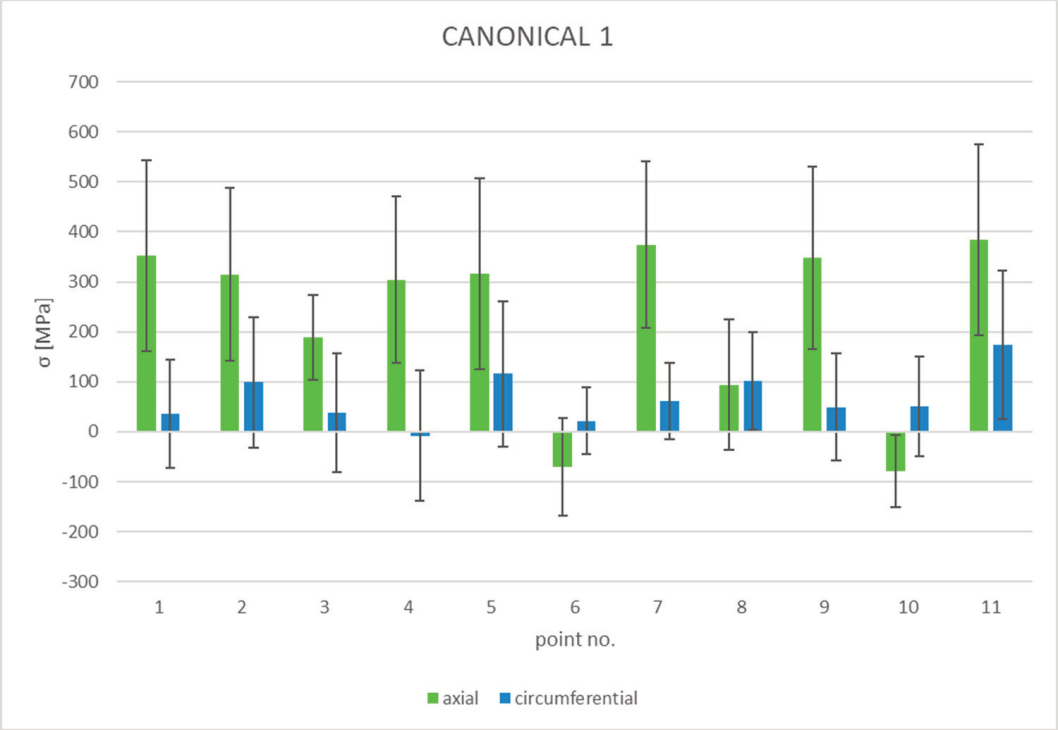

Figure 15. Results of X-ray diffraction stress measurements for specimen CANONICAL 1.

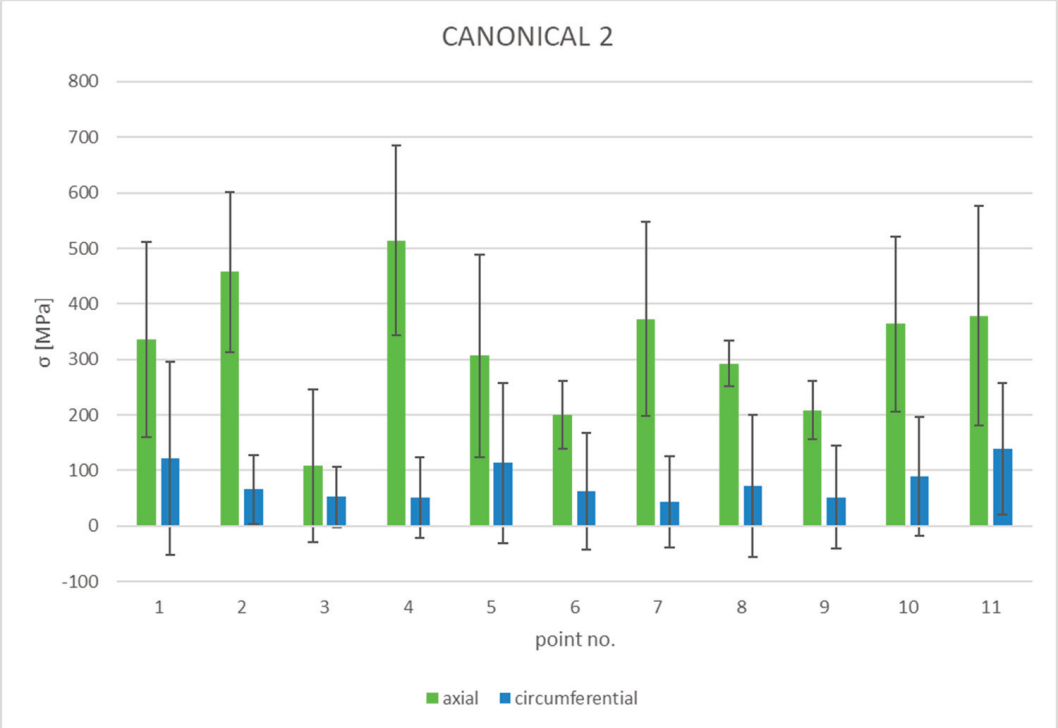

Figure 16. Results of X-ray diffraction stress measurements for specimen CANONICAL 2.

For most of the measurement points located on the surface of specimen CANONICAL 1, tensile stresses could be observed, with significantly higher values for the ‘axial’ direction. Significantly lower values were observed for the ‘circumferential’ direction. An interesting observation is the existence of stresses with significantly lower values for points located near the print platform, i.e. for points 3, 6, 8 and 10. This trend was observed for both the ‘axial’ and ‘circumferential’ directions, while for points 6 and 10 the stresses in the ‘axial’ direction even took on negative, i.e. compressive values.

Also in the case of specimen CANONICAL 2, as for specimen CANONICAL 1, stresses of a tensile nature were observed, with the stresses for the ‘axial’ direction having a much higher value than those for the ‘circumferential’ direction. For the ‘axial’ direction, the stresses change from about 100 MPa to 500 MPa, while for the ‘circumferential’ direction the change is between 50 MPa and 150 MPa. Moreover, in this case a decrease in the value of the measured stresses is observable; nevertheless, it is no longer as spectacular as in the case of CANONICAL 1, as there is no change in the nature of the stresses.

Stress measurements for the small arc specimens

For each of the small arc geometry specimens, five measurement points were located (see Figure 17). Also, for specimens with this geometry, two mutually perpendicular measurement directions were defined: ‘axial’ and ‘circumferential’. The measurement results are presented in Table 5 and in Figures 18–19.

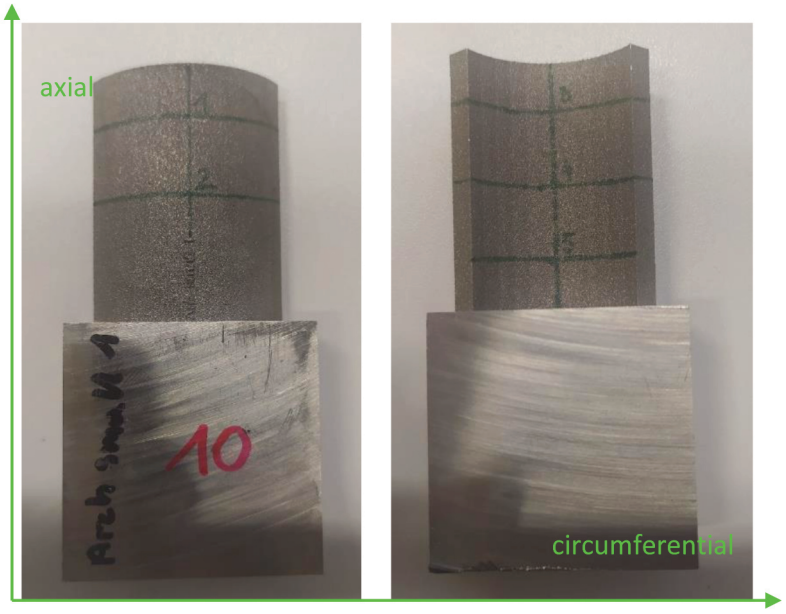

Figure 17. Speciment ARC SMALL 1, showing the location of measuring points on both sides.

Table 5. Results of X-ray diffraction stress measurements for ARC SMALL specimens.

point no. ↓	ARC SMALL 1				ARC SMALL 2			
	axial		circumferential		axial		circumferential	
	σ [MPa]	Δσ [Mpa]	σ [Mpa]	Δσ [Mpa]	σ [Mpa]	Δσ [Mpa]	σ [Mpa]	Δσ [Mpa]
1	417.9	214.7	49.3	107.2	355.6	173.9	44.9	160.6
2	372.3	187.4	78.1	94.8	317.3	158.3	39.7	132
3	307.7	194.9	220.9	94.6	319.8	164.5	346.5	185.1
4	425.3	195.1	196.7	90	424.7	175.3	286.3	129.1
5	359.6	26.5	130	74.9	225.7	60.6	178	110.9

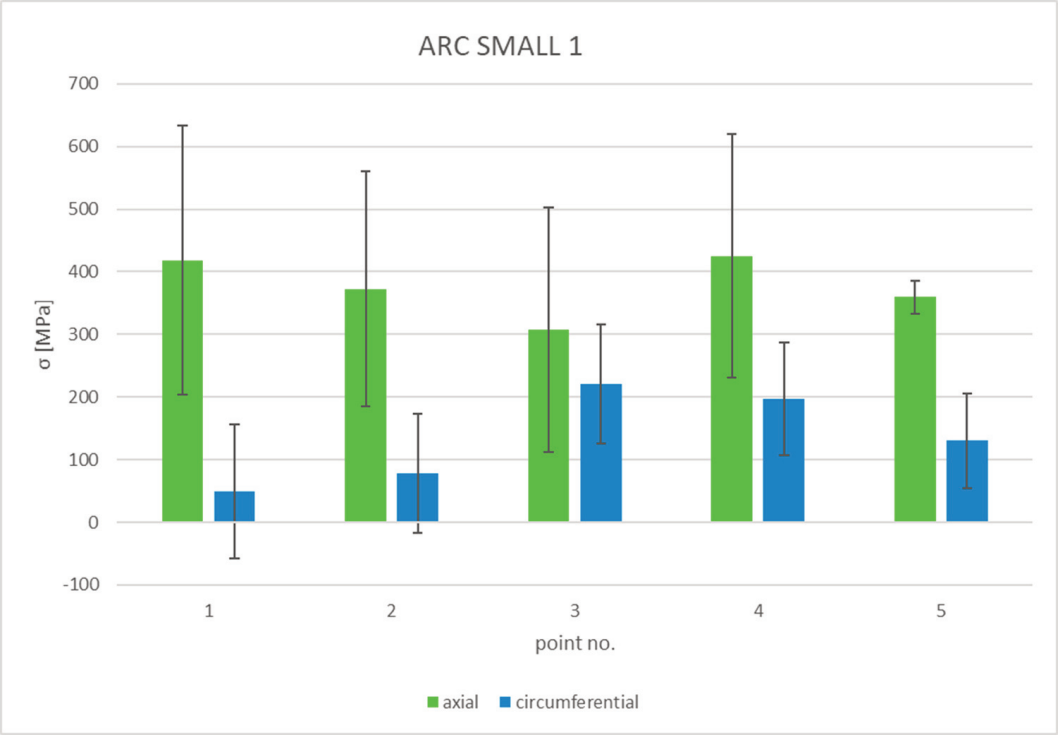

Figure 18. Results of X-ray diffraction stress measurements for specimen ARC SMALL 1.

The results of the stress measurements for specimen ARC SMALL 1 also indicate the presence of tensile stresses for all points and measurement directions. The stresses for the 'axial' direction ranged from about 300 MPa to just over 40 MPa. For the 'circumferential' direction, the stresses took on values in a wider range, i.e., from about 50 MPa to more than 200 MPa. Interestingly, there were much lower stresses for the circumferential direction on the convex side of the specimen i.e., for points 1 and 2. In addition, for the center point on the concave side of the specimen (no. 4), a higher value was observed for the 'axial' direction of stress.

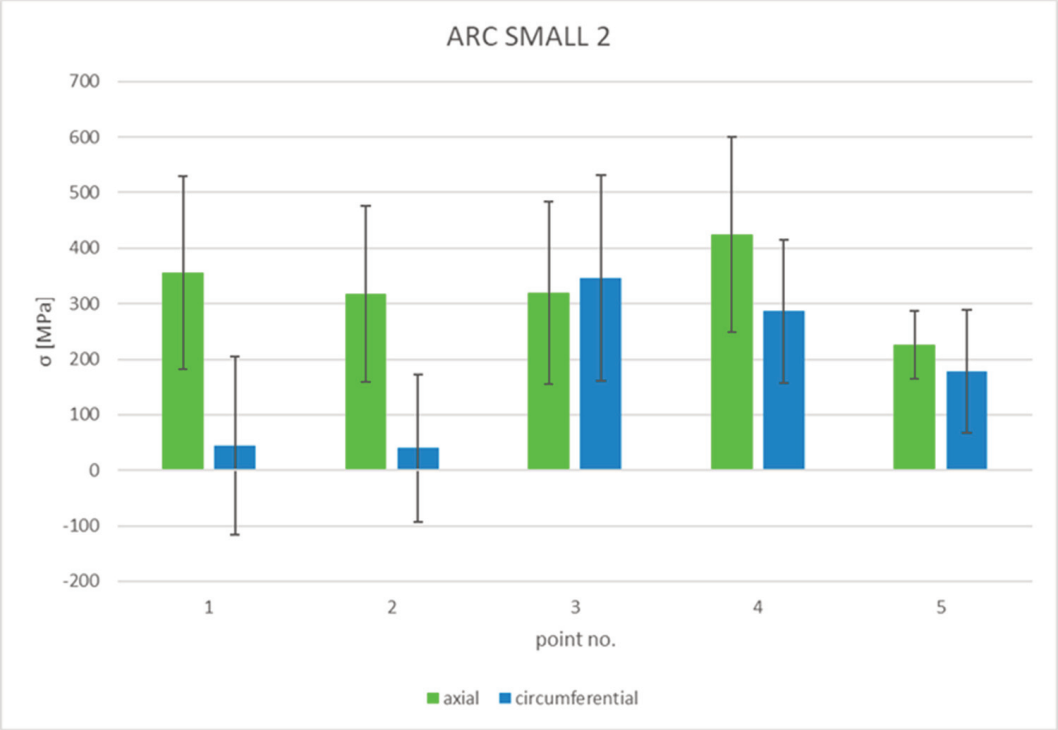

Figure 19. Results of X-ray diffraction stress measurements for specimen ARC SMALL 2.

The results of the measurements obtained for specimen ARC SMALL 2 are analogous to those for ARC SMALL 1. A similar trend is observable for the 'circumferential' direction of the measuring points located on the convex side of the specimen (they are significantly lower), as well as an apparent higher stress value in the 'axial' direction for point no. 4 on the concave side of the specimen.

Stress measurements for the large arc specimens

Diffraction measurements for the two large arc geometry specimens were realized for two directions for points numbered 1–9, and for the 'axial' only direction for points 12–14. For definition of the measurement points see Figure 20. Unfortunately, it was not possible to make measurements for the remaining points, i.e., 9–11 and 15–17, or for the 'circumferential' direction of points 12–14. This inability was revealed when the relatively complicated geometry of the sample was confronted with the diffractometer equipment geometry utilized for these series of experiments: for some measurement points, certain parts of the sample obscured either the incident or the reflected beam, making data acquisition impossible.

The measurement results for the two ARC BIG specimens are presented in Table 6 and Figure 21 and 22.

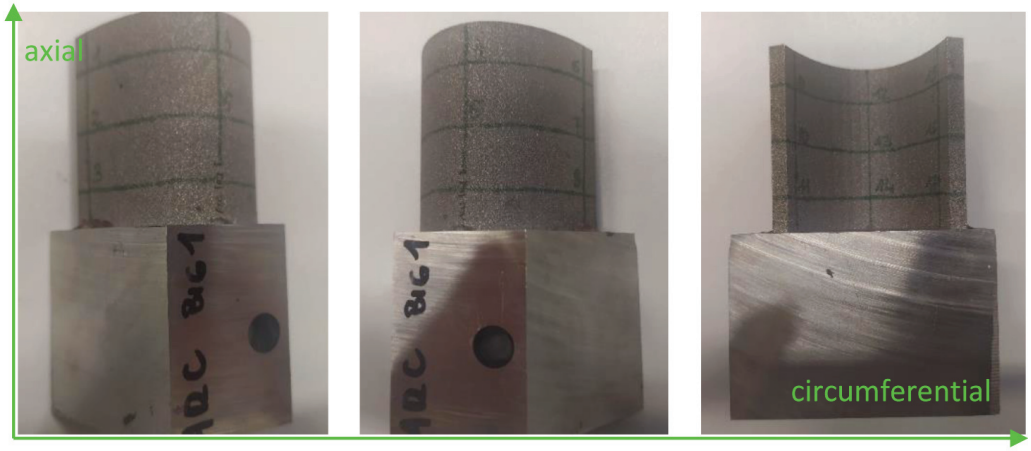

Figure 20. Specimen ARC BIG 1, showing the location of measuring points on both sides.

Table 6. Results of X-ray diffraction stress measurements for the two ARC BIG specimens. The measurements for points 9–11 and 15–17 for both directions, and for points 12–14 in the circumferential direction, could not be performed due to geometrical issues.

	ARC BIG 1				ARC BIG 2			
point no. ↓	axial		circumferential		axial		circumferential	
	σ [MPa]	Δσ [MPa]	σ [MPa]	Δσ [MPa]	σ [MPa]	Δσ [MPa]	σ [MPa]	Δσ [MPa]
1	341.8	161.7	220.1	162.2	352.7	156.8	186.2	160.4
2	313.1	194.9	227.7	152.6	366.5	171.9	249.6	192
3	342.2	189.4	224.4	179.5	340.3	87.2	-13.9	65.1
4	331.9	170	113.9	106	386.8	111.9	-24	116.9
5	355.8	169.5	56.9	118.3	313.7	151.1	18.5	126
6	403.3	180.3	45.3	60.4	379.9	175.6	209	183.2
7	412.1	171.2	98.7	137.1	392.7	183.7	46.5	60.5
8	341.3	132.8	10.7	52.4	226	112.4	198.9	84.6
12	599.2	128.1	-	-	712.9	104.4	-	-
13	485.1	81.4	-	-	450.1	61.3	-	-
14	297.7	59.6	-	-	191.6	28	-	-

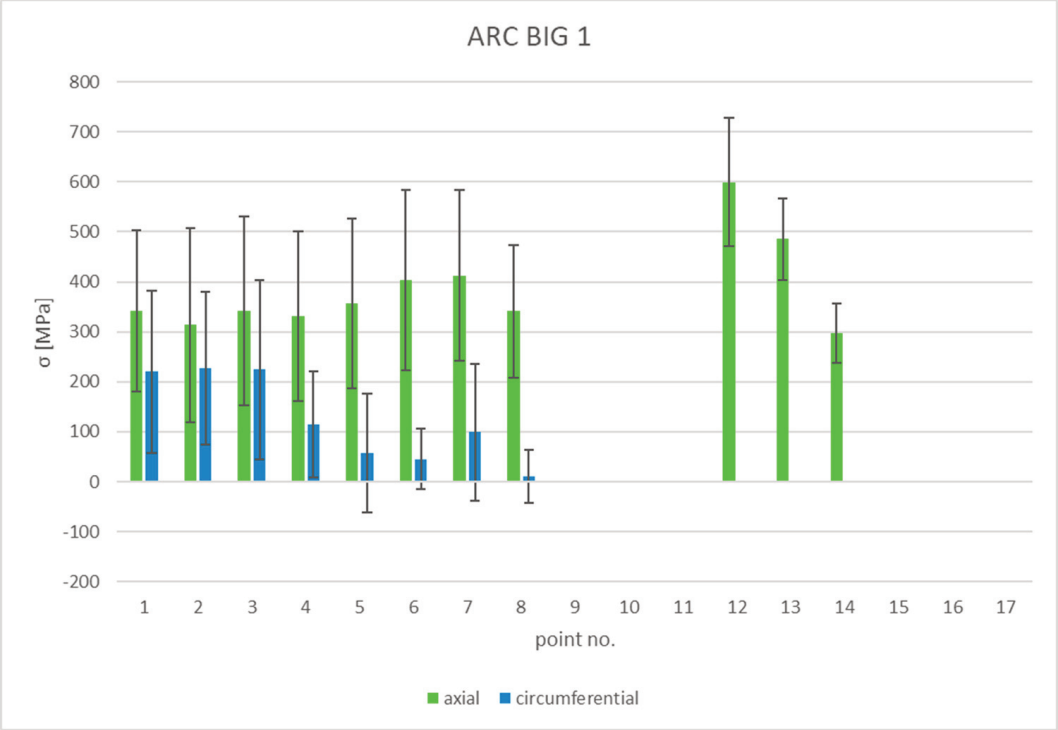

Figure 21. Results of X-ray diffraction stress measurements for specimen ARC BIG 1.

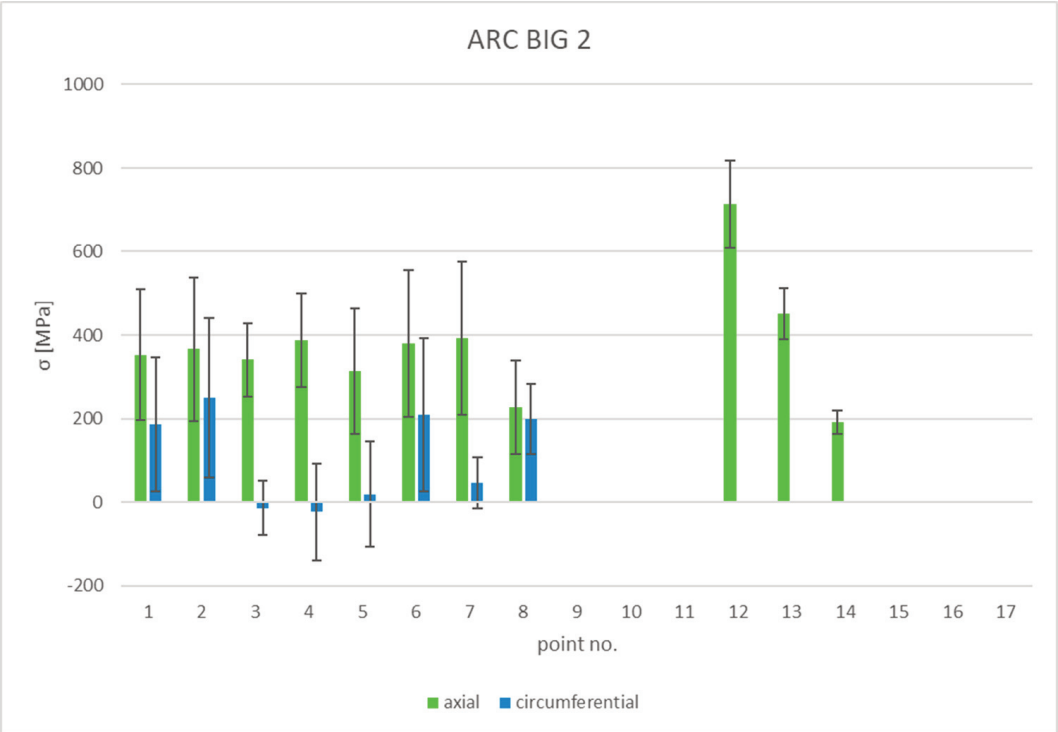

Figure 22. Results of X-ray diffraction stress measurements for specimen ARC BIG 2.

In the case of the ARC BIG 1 specimen, tensile stresses were observed for both measurement directions. Values were higher for the 'axial' direction, ranging from 300 MPa to 600 MPa, and significantly lower for the 'circumferential' direction, ranging from 0 MPa to about 200 MPa. An interesting distribution can be observed for the axial direction for points 12–14 located in the central part of the concave side of the specimen. The highest value is observed for the point closest to the edge of the specimen (no. 12) and the lowest for the point closest to the print platform (no. 14).

The stress values for the points located on specimen ARC BIG 2 were analogous to those obtained for specimen ARC BIG 1, with similar trends being observed. One observable difference, however, is a significant levelling of tensile stresses in the 'circumferential' direction for points 3–5 and 7.

Stress measurements for the blade-shaped specimen

On the blade-shaped specimen, 12 measuring points were evenly distributed on one side. As for the previous samples, the measurements were carried out for two mutually perpendicular directions (see Figure 23).

Figure 23. Specimen BLADE 2, showing the location of measuring points.

The X-ray diffraction stress measurements for this specimen are presented in Table 7 and in Figure 24.

Table 7. Results of X-ray diffraction stress measurements for specimen BLADE 2.

point no. ↓	axial		circumferential	
	σ [MPa]	Δσ [MPa]	σ [MPa]	Δσ [MPa]
1	591	80.1	163.6	160
2	518.7	196.3	209.6	180.2
3	405.4	266.3	158.6	126.2
4	305.5	143.7	132.1	106.8
5	426.4	43.7	270.1	129.9
6	389.8	74.8	176.5	78.7
7	485.4	176.7	236	150.5
8	495	185.7	61.5	34.9
9	21	47.5	219.7	184.7
10	107.8	29.1	219.9	165.2
11	147.4	17.2	282.6	150.7
12	244.3	36.6	218.4	142.8

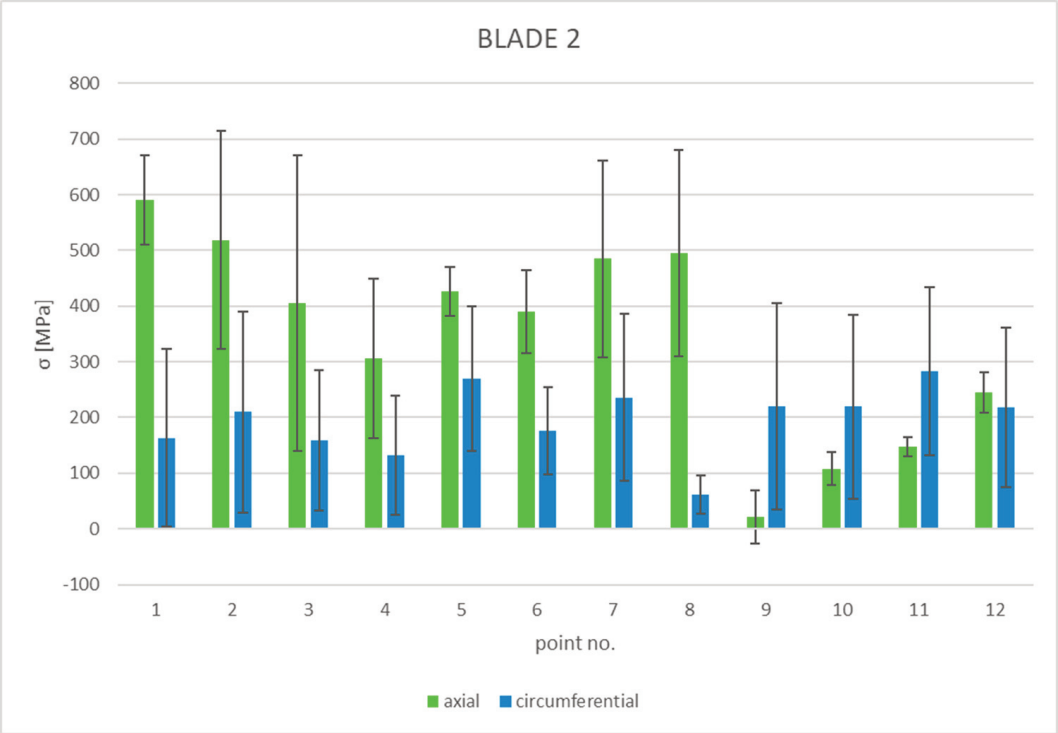

Figure 24. Results of X-ray diffraction stress measurements for specimen BLADE 2.

Significant tensile stresses were also observed for this specimen, particularly in the 'axial' direction for points 1–8, which are further away from the printing platform than points 9–12. For points 1–8, the stress measurements for the 'axial' direction showed stresses in the range of 300 MPa to 600 MPa, while for the 'circumferential' direction the stress values ranged from approx. 50 MPa to approx. 250 MPa. A completely different stress distribution was observed for points close to the print platform i.e., 9–12. For these points, the stress values for the 'circumferential' direction were higher, ranging from approx. 200 MPa to approx. 300 MPa. The stresses in the 'axial' direction, on the other hand, were not higher than 250 MPa. Once again, a trend towards lower stress values near the print platform is observed (a trend previously observed for specimens CANONICAL 1, ARC SMALL 1, ARC SMALL 2).

5. MEASUREMENT UNCERTAINTY

Measurement uncertainty is a non-negligible aspect of any experimental work. In the series of diffraction experiments reported herein, carried out to identify the level of stress in components made using incremental methods, relatively high levels of measurement uncertainty were observed, averaging around 137 MPa. Such a high level of measurement uncertainty probably stems from the complex nature of the material itself, which is a non-trivial material from the perspective of diffraction measurement: during diffraction reflection acquisition, overlapping of reflections from planes of different phases were observed. In addition, each of the specimens was characterized by significant roughness, which had a substantial effect on the experimentally undesired scattering of incident radiation. Unfortunately, despite using optimized measurement parameters and half-automatic measurement analyses that allowed for the identification stress levels in finite time for such a large number of unit measurements, effective separation of these diffraction reflections was unattainable.

To mitigate measurement errors, various methodological and technological solutions used in diffraction methodology were applied, such as the OMEGA measurement mode and focusing lenses on the incident beam path, which allow the full radiating power of the X-ray tube to be used and the influence of sample roughness to be negated. Moreover, the lenses facilitated the generation of a parallel beam, which substantially lowered the influence of the surface roughness. In addition, a fast semiconductor detector was used.

Despite the measurement uncertainty, however, consistent trends observed in the measurement results lend credence to the reliability of the experimental results obtained over the entire measurement cycle.

6. CONCLUSIONS

Stress measurements were performed on 10 specimens made using incremental methods from Inconel 718 alloy, across 92 different points on their surface. A total of 178 stress measurements were made using the $\sin^2\psi$ method, for different measurement directions defined with respect to the geometry of the specimens. Preliminarily to the main measurement cycle, a phase analysis of the material was performed. It was found

that detaching a specimen from the print platform could not be performed without changing the stress state, and the stress measurement parameters were optimized.

Summarizing the results of the obtained measurements, the following conclusions can be drawn:

- The Inconel 718 alloy exhibits a multiphase structure predominantly characterized by a cubic FCC phase. However, it also contains precipitations in the form of niobium-nickel compounds with varying crystallographic structures.
- Cutting off the sample from the printing platform causes a change in the stress state and induces tensile stresses in the longitudinal direction relative to the printing platform. The stresses in the perpendicular direction are also changed by severing the specimen from the platform. As a result, it is not possible to cut off printed specimens from the platform without introducing changes to the stress state.
- Tensile stresses were observed for all specimens examined. For specimens with flat geometries the stresses for both directions had similar values, while for specimens with curved geometries the stresses for the 'axial' direction had significantly higher values than for the 'circumferential' direction.
- For some samples, lower stress values were observed in the close vicinity of the printing platform (CANONICAL 1, ARC SMALL 1, ARC SMALL 2). For some there was even a relative decrease in stress values in the 'axial' direction and an increase in stress in the circumferential direction near the printing platform (BLADE 2).

Acknowledgment

This work was financially supported by a grant from the Regional Operational Programme for the Mazowieckie Voivodeship 2014–2020, under the framework of project no. RPMA.01.02.00-14-B479/18 entitled *Development and implementation of an innovative design service for turbojet engines using additive technology and advanced cooling methods.*

References

Amato, K.N., Gaytan, S.M., Murr, L.E., Martinez, E., Shindo, P.W., Hernandez, J., Collins, S., Medina, F. (2012). Microstructures and mechanical behavior of Inconel 718 fabricated by selective laser melting. *Acta Materialia*, *60*(5), 2229–2239. https://doi.org/10.1016/j.actamat.2011.12.032

Ardila, L.C., Garciandia, F., González-Díaz, J.B., Álvarez, P., Echeverria, A., Petite, M.M., Deffley, R., Ochoa, J. (2014). Effect of IN718 Recycled Powder Reuse on Properties of Parts Manufactured by Means of Selective Laser Melting. *Physics Procedia*, *56*, 99–107. https://doi.org/10.1016/j.phpro.2014.08.152

Blackwell, P. L. (2005). The mechanical and microstructural characteristics of laser-deposited IN718. *Journal of Materials Processing Technology*, *170*(1), 240–246. https://doi.org/10.1016/j.jmatprotec.2005.05.005

Burke, M. G., & Miller, M. K. (1991). Precipitation in Alloy 718: A combined AEM and APFIM Investigation. In E.A. Loria (Ed), *Superalloys 718, 625 and Various Derivatives* (pp. 337–350). TMS. https://doi.org/10.7449/1991/Superalloys_1991_337_350

Ezugwu, E. O. (2004). High speed machining of aero-engine alloys. *Journal of the Brazilian Society of Mechanical Sciences and Engineering*, *26*(1), 1–11. https://doi.org/10.1590/S1678-58782004000100001

Ferreri, N. C., Vogel, S. C., & Knezevic, M. (2020). Determining volume fractions of γ, γ′, γ″, δ, and MC-carbide phases in Inconel 718 as a function of its processing history using an advanced neutron diffraction procedure. *Materials Science and Engineering: A*, *781*, 139228. https://doi.org/10.1016/j.msea.2020.139228

Gadalińska, E., Michałowski, A., & Czarnewicz, S. (2019). Determination of Stress Values in the Surface Layer of Inconel 718 Samples Dedicated to Fatigue Tests. *Fatigue of Aircraft Structures*, *2019*(11), 78–86. https://doi.org/10.2478/fas-2019-0008

Ghorbanpour, S., Deshmukh, K, Sahu, S., Riemslag, T., Reinton, E., Borisov, E., Popovich, A., Bertolo, V., Jiang, Q., Sanchez, M. T., Knezevic, M., & Popovich, V. (2022). Additive manufacturing of functionally graded inconel 718: Effect of heat treatment and building orientation on microstructure and fatigue behaviour. *Journal of Materials Processing Technology*, *306*, 117573. https://doi.org/10.1016/j.jmatprotec.2022.117573

Gribbin, S., Ghorbanpour, S., Ferreri, N. C., Bicknell, J., Tsukrov, I., & Knezevic, M. (2019). Role of grain structure, grain boundaries, crystallographic texture, precipitates, and porosity on fatigue behavior of Inconel 718 at room and elevated temperatures. *Materials Characterization*, *149*, 184–197. https://doi.org/10.1016/j.matchar.2019.01.028

Hilley, M. E. (Ed.). (1971). *Residual stress measurement by X-ray diffraction-SAE J784a*. Society of Automotive Engineers.

Hönnige, J., Seow, C.E., Ganguly, S., Xu, X., Cabeza, S., Coules, H., & Williams, S. (2021). Study of residual stress and microstructural evolution in as-deposited and inter-pass rolled wire plus arc additively manufactured Inconel 718 alloy after ageing treatment. *Materials Science and Engineering: A*, *801*, 140368. https://doi.org/10.1016/j.msea.2020.140368

Hosseini, E., & Popovich, V. A. (2019). A review of mechanical properties of additively manufactured Inconel 718. *Additive Manufacturing*, *30*, 100877. https://doi.org/10.1016/j.addma.2019.100877

Huang, X., Chaturvedi, M. C., & Richards, N. L. (1996). Effect of homogenization heat treatment on the microstructure and heat- affected zone microfissuring in welded cast alloy 718. *Metallurgical and Materials Transactions A*, *27*(3), 785–790. https://doi.org/10.1007/BF02648966

Kruth, J. P. (1991). Material Incress Manufacturing by Rapid Prototyping Techniques. *CIRP Annals*, *40*(2), 603–614. https://doi.org/10.1016/S0007-8506(07)61136-6

Liu, F., Lin, X., Yang, G., Song, M., Chen, J., & Huang, W. (2011). Microstructure and residual stress of laser rapid formed Inconel 718 nickel-base superalloy. *Optics & Laser Technology*, *43*(1), 208–213. https://doi.org/10.1016/j.optlastec.2010.06.015

Malicki, M., Gadalińska, E., & Chmiel, M. (2016). The Impact of Damage in Anneling Inconel 718 on Hardness Measured by the Vickers Method. *Fatigue of Aircraft Structures*, *2016*(8), 92–96. https://doi.org/10.1515/fas-2016-0007

Mercelis, P., & Kruth, J.-P. (2006). Residual stresses in selective laser sintering and selective laser melting. *Rapid Prototyping Journal*, *12*(5), 254–265. https://doi.org/10.1108/13552540610707013

Mostafa, A., Rubio, I. P., Brailovski, V., Jahazi, M., & Medraj, M. (2017). Structure, Texture and Phases in 3D Printed IN718 Alloy Subjected to Homogenization and HIP Treatments. *Metals*, *7*(6), 196. https://doi.org/10.3390/met7060196

Nezhadfar, P. D., Johnson, A. S., & Shamsaei, N. (2020). Fatigue behavior and microstructural evolution of additively manufactured Inconel 718 under cyclic loading at elevated temperature. *International Journal of Fatigue*, *136*, 105598. https://doi.org/10.1016/j.ijfatigue.2020.105598

Pinkerton, A. J., & Li, L. (2004). Modelling the geometry of a moving laser melt pool and deposition track via energy and mass balances. *Journal of Physics D: Applied Physics*, *37*(14), 1885. https://doi.org/10.1088/0022-3727/37/14/003

Popovich, V. A., Borisov, E. V., Popovich, A. A., Sufiiarov, V. Sh., Masaylo, D. V., & Alzina, L. (2017). Impact of heat treatment on mechanical behaviour of Inconel 718 processed with tailored microstructure by selective laser melting. *Materials & Design*, *131*, 12–22. https://doi.org/10.1016/j.matdes.2017.05.065

Prevey, P. S. (1986). *X-ray diffraction residual stress techniques*. Lambda Technologies.

Radhakrishna, C., & Prasad Rao, K. (1997). The formation and control of Laves phase in superalloy 718 welds. *Journal of Materials Science*, *32*(8), 1977–1984. https://doi.org/10.1023/A:1018541915113

Sanchez, S., Gaspard, G., Hyde, C. J., Ashcroft, I. A., Ravi, G. A., & Clare, A. T. (2021). The creep behaviour of nickel alloy 718 manufactured by laser powder bed fusion. *Materials & Design*, *204*, 109647. https://doi.org/10.1016/j.matdes.2021.109647

Sharman, A. R. C., Hughes, J. I., & Ridgway, K. (2006). An analysis of the residual stresses generated in Inconel 718TM when turning. *Journal of Materials Processing Technology*, *173*(3), 359–367.

Shiomi, M., Osakada, K., Nakamura, K., Yamashita, T., & Abe, F. (2004). Residual Stress within Metallic Model Made by Selective Laser Melting Process. *CIRP Annals*, *53*(1), 195–198. https://doi.org/10.1016/S0007-8506(07)60677-5

Standard EN 15305:2008. (2008). *Non-destructive testing – Test method for residual stress analysis by X-ray diffraction*.

Sui, S., Chen, J., Fan, E., Yang, H., Lin, X., & Huang, W. (2017). The influence of Laves phases on the high-cycle fatigue behavior of laser additive manufactured Inconel 718. *Materials Science and Engineering: A*, *695*, 6–13. https://doi.org/10.1016/j.msea.2017.03.098

Wang, X., Gong, X., & Chou, K. (2017). Review on powder-bed laser additive manufacturing of Inconel 718 parts. *Proceedings of the Institution of Mechanical Engineers, Part B: Journal of Engineering Manufacture*, *231*(11), 1890–1903. https://doi.org/10.1177/0954405415619883

Yao, C. F., Jin, Q. C., Huang, X. C., Wu, D. X., Ren, J. X., & Zhang, D. H. (2013). Research on surface integrity of grinding Inconel718. *International Journal of Advanced Manufacturing Technology*, *65*(5), 1019–1030. https://doi.org/10.1007/s00170-012-4236-7